

Determination of Temperature- and Carrier-Dependent Surface Recombination in Silicon

Anh Huy Tuan Le,^{*} Shuai Nie, Eduardo Prieto Ochoa, John Rodriguez, Ruy Sebastian Bonilla, and Ziv Hameiri

Knowledge regarding the temperature dependence of the surface recombination at the interface between silicon and various dielectrics is critically important as it 1) provides fundamental information regarding the interfaces and 2) improves the modeling of solar cell performance under actual operating conditions. Herein, the temperature- and carrier-dependent surface recombination at the silicon–oxide/silicon and aluminum–oxide/silicon interfaces in the temperature range of 25–90 °C using an advanced technique is investigated. This method enables to control the surface carrier population from heavy accumulation to heavy inversion via an external bias voltage, allowing for the decoupling of the bulk and surface contributions to the effective lifetime. Thus, it offers a simple and versatile manner to separate the chemical passivation from the charge-assisted population control at the silicon/dielectric interface. A model is established to obtain the temperature dependence of the capture cross sections, a critical capability for the optimization of the dielectric layers and the investigation of the fundamental properties of the passivation under field operating conditions.

1. Introduction

Minimizing the recombination within the bulk and at the surfaces of silicon (Si) solar cells is a crucial factor in enhancing their performance.^[1] Modern solar cells are designed to be thinner to reduce costs^[2] and enhance their open-circuit voltage (V_{oc}), thereby improving their efficiency.^[3] As the bulk quality of Si wafers has been significantly improved in recent years,^[4] the performance of these solar cells has become more sensitive to

surface recombination,^[5] making the reduction of this loss mechanism exceptionally important.


Surface recombination arises from dangling bonds caused by the abrupt discontinuity of the Si crystal lattice at this interface.^[6] It can be mitigated through surface passivation processes, which aim to reduce the density of interfacial defects (D_{it}) and/or control the carrier populations near the Si surface.^[7] The former can be achieved by saturating the dangling bonds with an additional dielectric layer or chemical species like hydrogen.^[6] Consequently, this process is often referred to as “chemical passivation”.^[7] The latter can be accomplished through methods such as doping, introducing fixed charges (Q_f) in the dielectric films, or controlling the materials’ work function.^[8] All these approaches aim to amplify the imbalance

between the concentrations of electrons and holes near the Si surface (n_s and p_s , respectively) and hence, reduce the surface recombination rate.^[7] Among these methods, introducing fixed charges near the Si surface is an effective and widely adopted approach. It is typically applied to commercial solar cells by depositing layers with fixed charges onto the Si surface.^[9–15] Common materials used for these applications include dielectric films with positive fixed charges, such as silicon dioxide (SiO_2)^[9,12,13] and silicon nitride (SiN_x)^[10,14,16] or those with negative fixed charges, such as aluminum oxide (AlO_x)^[6,17,18]. These films not only facilitate carrier population control through their fixed charges (referred to as charge-assisted population control) but also contribute to chemical passivation. Recently, these films have also been used as a part of passivating contacts.^[19–25] A notable example is the use of silicon oxide (SiO_x) in tunnel oxide passivated contacts (TOPCon).^[25] Therefore, gaining a deeper understanding of surface carrier population control is of critical importance for further advancements in surface passivation and carrier selectivity.

A commonly employed technique for investigating the impact of surface carrier populations on recombination statistics at the Si surface is based on corona discharge deposition.^[26–30] However, this technique comes with several drawbacks. Measuring the concentration of deposited corona discharge requires a chamber equipped with a Kelvin probe. This setup leads to frequent transfers of samples between the chamber and measurement tool, significantly prolonging the process. Another concern is the stability

A. H. T. Le, S. Nie, E. P. Ochoa, J. Rodriguez, Z. Hameiri
School of Photovoltaic and Renewable Energy Engineering
University of New South Wales
Sydney, NSW 2052, Australia
E-mail: huytuananh.le@unsw.edu.au

R. S. Bonilla
Department of Materials
University of Oxford
Oxford OX1 3PH, UK

 The ORCID identification number(s) for the author(s) of this article can be found under <https://doi.org/10.1002/solr.202400191>.

© 2024 The Author(s). Solar RRL published by Wiley-VCH GmbH. This is an open access article under the terms of the Creative Commons Attribution-NonCommercial-NoDerivs License, which permits use and distribution in any medium, provided the original work is properly cited, the use is non-commercial and no modifications or adaptations are made.

DOI: 10.1002/solr.202400191

of corona charges on dielectric layers.^[27] Furthermore, there is uncertainty regarding the influence of temperature-dependent measurements on charge stability. To address these issues, several alternative methods have been proposed.^[31–37] These methods involve controlling surface carrier populations during measurements by applying bias voltages to metal contacts on the sample. However, these approaches require an additional vacuum-based process for creating these metal contacts. Recently, Bonilla^[38] introduced a novel alternative method with rapid sample preparation. This method applies a bias voltage to the sample via semitransparent gates made from PEDOT:PSS [poly(3,4-ethylenedioxythiophene)-poly(styrenesulfonate)] to control carrier populations near Si surfaces during photoconductance (PC) decay measurements. Notably, this technique allows for the investigation of surface recombination across a wide range of surface potentials. By applying this technique, Bonilla^[38] investigated the recombination statistics at the interfaces between Si substrates and different dielectric layers. However, that study only provides information at room temperature (25 °C), which does not reflect the realistic operating temperatures of solar cells in the field. Furthermore, it has yet to explore other crucial parameters such as the bulk Shockley–Read–Hall lifetime ($\tau_{\text{bulk,SRH}}$), D_{it} , and the temperature dependence of capture cross sections of electrons and holes (σ_n and σ_p , respectively).

This study aims to extend the capabilities of this method by investigating the temperature dependence of the recombination at the SiO_2/Si and AlO_x/Si interfaces. Additionally, an advanced model is established for extracting the surface defect parameters.

2. Experimental Section

2.1. Sample Preparation

In this study, symmetrical lifetime test structures passivated by either SiO_2 or AlO_x films were investigated. The information regarding the used wafers and films is summarized in **Table 1**. These wafers were first cleaned using the Radio Corporation of America procedures^[39] followed by immersion in 5% diluted hydrofluoric acid (HF). The fabrication of the AlO_x samples employed an industrial plasma-enhanced chemical vapor deposition (PECVD) system (MAiA XS, Meyer Burger). Nitrous oxide (N_2O) and tri-methyl aluminum (TMA) were used as process

gases, with argon (Ar) serving as a carrier gas for the TMA. The deposition process was carried out at 350 °C. After deposition, the samples underwent annealing at 425 °C in air for 15 min. Meanwhile, the SiO_2 films were formed by thermal oxidation using a tube furnace in a dry dichloroethylene/oxygen atmosphere without a post-annealing process.

Semitransparent gates were formed by painting the PEDOT:PSS solution (1.1% in water, from Sigma-Aldrich) on both surfaces of the test structures, followed by a curing process at 80 °C for 2 min in air ambient using a hot plate.^[40] The resistance of the PEDOT:PSS layers was confirmed to be within the desired range of 6–10 k Ω using a multimeter. To create the metal contacts on one side of the test structures (hereafter referred to as the “front side”), a $0.5 \times 0.5 \text{ cm}^2$ area of the dielectric layers was removed from the corner of the samples using a diamond pen. A gallium/indium eutectic (EGaIn, 75.5% Ga, 24.5% In, from Sigma-Aldrich) paste was then applied to this area, followed by a silver (Ag) paint layer. The procedure of sample preparation is shown in **Figure 1**.

2.2. Characterization

2.2.1. Measurement Setup

A sketch of the measurement setup used in this study is depicted in **Figure 2**. The sample was placed on a temperature-controlled stage of a WCT-120TS lifetime tester (from Sinton Instruments). A probe and a copper wire were employed to establish connections between the front and rear PEDOT:PSS gates and one of the terminals of a direct current (DC) power supply. Simultaneously, a second probe linked the metal contact to the second terminal. The manipulation of surface carrier populations was achieved by applying bias voltages, ranging from –25 to +15 V, provided by the DC power supply. An additional set of probes was affixed to the front PEDOT:PSS gate and the metal contact to monitor the actual voltage applied to the sample. Upon comparison, it was observed that the measured voltages closely mirrored the supplied voltages, particularly when the voltage was below 10 V. Beyond this threshold, a slight reduction in the measured voltage compared to the supplied voltage was noted. This voltage discrepancy became more prominent with an increase in the supplied voltage; however, it remained below 10% throughout the investigated voltage range.

2.2.2. Measurements of Effective Lifetime (τ_{eff})

The τ_{eff} measurements were conducted in a temperature range from 25 to 90 °C. The uncertainty associated with the cell temperature during the measurements was estimated at ± 0.2 °C. The transient mode was selected for measurements of samples with sufficiently high τ_{eff} [$> 200 \mu\text{s}$ at the excess carrier concentration (Δn) of 10^{15} cm^{-3}], whereas the quasisteady-state (QSS) mode was used for measurements of samples with lower τ_{eff} . To confirm that the samples were stable during the measurements, τ_{eff} measurements before and after the bias voltage scan were done. A similar stability test was performed before and after each of the temperature scans.

Table 1. Wafers and passivation films used in this study.

		Sample	
Substrate	Type	SiO_2	AlO_x
		p-type FZ	n-type Cz
	Doping [$\Omega\text{-cm}$]	$(1.5\text{--}1.7) \times 10^{16}$	$(4.5\text{--}5.4) \times 10^{14}$
	Thickness [nm]	480 ± 10	180 ± 10
	Surface	Polished	Planarized
Film	Deposition method	Thermal oxidation	PECVD
	Thickness [nm]	100	90

FZ: Float zone.

Cz: Czochralski.

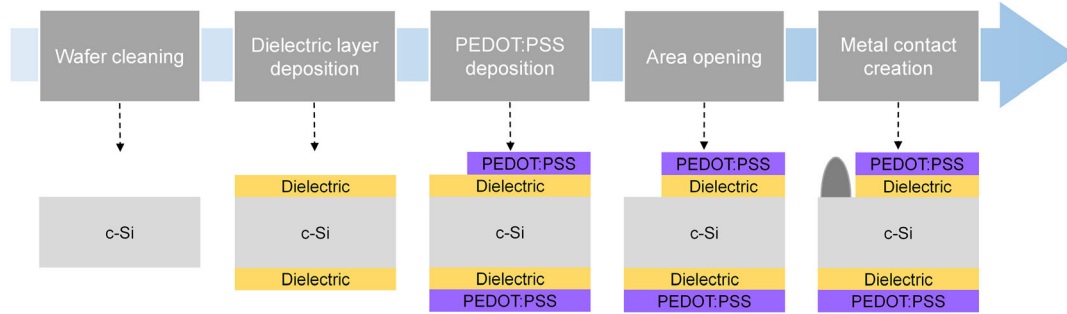


Figure 1. Procedure of sample preparation.

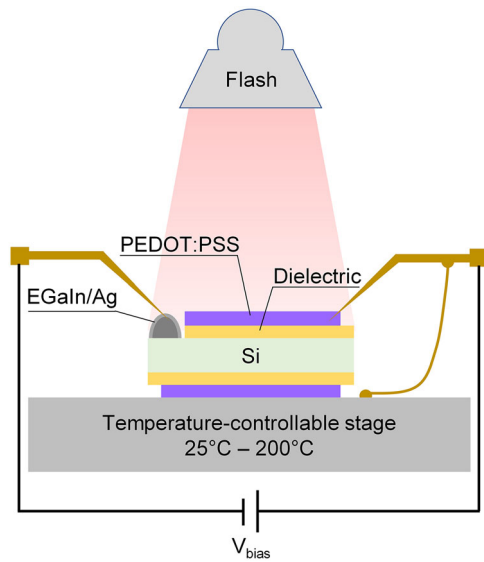


Figure 2. Sketch of measurement setup and test structure.

The optical constant significantly influences QSS τ_{eff} measurements, as it impacts the estimation of the amount of incident light that is absorbed in the sample. In contrast, measurements using the transient mode are independent of the generation rate (G) and, therefore, the optical constant. Given the semitransparent nature of the PEDOT:PSS layers, it is imperative to account for their absorption characteristics. The optical constant can be estimated by matching τ_{eff} measurements obtained from the QSS and transient modes. **Figure 3** presents τ_{eff} as a function of Δn obtained from the QSS and transient measurements of the symmetric AlO_x lifetime test structure at a bias voltage of 3 V. This bias voltage value was selected to ensure a τ_{eff} value that is appropriate for both modes ($>200 \mu\text{s}$ at $\Delta n = 10^{15} \text{ cm}^{-3}$). The τ_{eff} measured by the QSS mode with an optical constant of 0.7 (default value) was significantly lower than the τ_{eff} obtained by the transient mode. To match these curves, the optical constant was adjusted to 0.36. This value was also tested and found to be suitable for various AlO_x samples. While applying this approach to estimate the optical constant of the studied symmetrical SiO_2 lifetime test structures proves challenging, as their τ_{eff} is below $200 \mu\text{s}$ (at $\Delta n = 10^{15} \text{ cm}^{-3}$) for the entire bias voltage range, it was assumed that the same optical constant can be also applied to these samples.

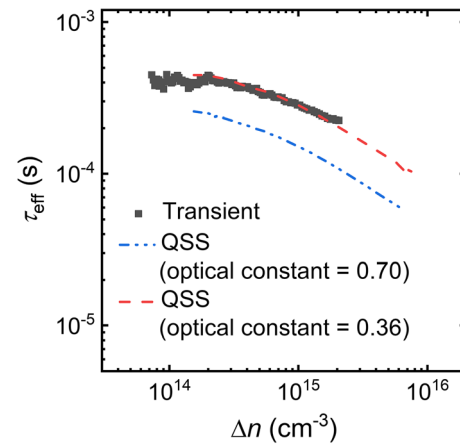


Figure 3. Transient and QSS τ_{eff} measurements of the symmetrical AlO_x lifetime test structure at a bias voltage of 3 V. The optical constants of 0.70 and 0.36 are the default and adjusted values, respectively.

2.3. Modeling

An advanced model^[41] based on the extended Shockley-Read-Hall (SRH) formalism^[42] and the iterative algorithms of Girisch et al.^[35] and Aberle et al.^[43] was established. The effect of charge fluctuations (σ_q)^[41] was also incorporated into the model. The Si space-charge density was determined based on the methods presented in refs. [42,44]. As an external bias voltage influences solely the surface carrier populations, τ_{eff} variation with the bias voltage provides information about the impact of the charge on the surface recombination (U_s) which is described by^[45]

$$U_s = \int_{E_v}^{E_c} \frac{(n_s p_s - n_i^2)}{\frac{(n_s + n_1(E))}{\nu_{\text{thp}} D_h(E) \sigma_p} + \frac{(p_s + p_1(E))}{\nu_{\text{thn}} D_n(E) \sigma_n}} dE \quad (1)$$

$$n_1 = n_i \exp\left(\frac{E_t - E_i}{k_B T}\right) \text{ and } p_1 = n_i \exp\left(\frac{E_i - E_t}{k_B T}\right) \quad (2)$$

where E_c is the conduction band edge, E_v is the valence band edge, n_i is the Si intrinsic carrier concentration,^[46] ν_{thp} (ν_{thn}) is the thermal velocity of hole (electron)^[47,48] (see Appendix A for more details), n_1 (p_1) is the equilibrium densities of electrons (holes) when the Fermi level coincides with the defect energy

level (E_i), E_i is the intrinsic Fermi level, k_B is the Boltzmann constant, and T is the temperature.

The input parameters of this model are as follows:

- 1) The doping type, measured resistivity (ρ), and thickness of wafers (see Table 1).
- 2) The thickness of dielectric films (see Table 1).
- 3) The gate charge (Q_{gate}) that is determined using:^[38]

$$Q_{\text{gate}} = \frac{\epsilon_0 K_{\text{ins}}}{t_{\text{ins}}} \left(V_{\text{gate}} - \frac{\phi_{\text{MS}}}{q} \right) \quad (3)$$

where ϵ_0 is the vacuum permittivity, K_{ins} is the layer's dielectric constant, and t_{ins} is the dielectric layer's thickness; $\epsilon_0 K_{\text{ins}}/t_{\text{ins}}$ is the insulator stack capacitance. V_{gate} is the bias voltage, ϕ_{MS} is the work function difference between the Si and the PEDOT: PSS, and q is the electric charge.

The insulator stack capacitances reported for the SiO_2 and AlO_x films in ref. [38] were used in this study. The ϕ_{MS} values were calculated from the work functions of Si (5.03 and 4.38 eV for the used p- and n-type Si wafers, respectively) and PEDOT: PSS (4.85 eV); they were determined to be -0.18 and 0.47 eV for the test structures with SiO_2 and AlO_x layers, respectively.

- 4) Q_f which can be estimated from Q_{gate} :

$$Q_f = -(Q_{\text{gate}} + Q_{\text{Si}}) \quad (4)$$

where Q_{Si} is the charge at the Si surface, including Si/dielectric interface states (Q_{it}) and the space-charge region (Q_{SCR}). Typically, at the point of maximum recombination, these charges were estimated to be $2 \times 10^{11} \text{ q cm}^{-2}$.^[38,43,49–51] The estimated Q_f was then compared to the measured Q_f obtained by the capacitance–voltage (C – V) method.^[52]

5) $\tau_{\text{bulk,SRH}}$ which can be estimated from the regimes of very positive (for SiO_2) or very negative (for AlO_x) bias voltages. In these regimes, τ_{eff} is limited by the bulk recombination. This capability of the used method will be discussed in detail in the following section.

6) Defect distributions (see Appendix B). In the previous study,^[53] a model with one midgap defect was established. In this study, both donor-like and acceptor-like defects with top-hat distributions were used. The Si/ SiO_2 interface defect distributions, as reported in refs. [51,54], were utilized such that the overall defect densities were representative of a physical interface. Our recent study demonstrated that these distributions can also be used for defects at the Si/ AlO_x interface,^[8] as a SiO_x layer is usually present between the Si wafer and the AlO_x film deposited by ALD systems.^[55]

7) Tail states for both the SiO_2 and AlO_x interfaces.^[8,51] Note that the width of the tail distribution is defined as the energy gap between the band edge and the energy at which the defect density decreases to below $10^8 \text{ cm}^{-2} \cdot \text{eV}^{-1}$.

The input parameters are summarized in Table 2. The estimated Q_f and $\tau_{\text{bulk,SRH}}$ will be presented in the next sections along with a comparison to the values determined from other methods.

To reproduce the trend of τ_{eff} as a function of the bias voltage, the D_{it} values of both the donor-like and acceptor-like defects were fit to match the minimum τ_{eff} point; the D_{it} values of the tail states and the capture cross sections of both donor-like

Table 2. Defect type, its distribution function, width, and energy level used as input parameters in the model.

	Donor tail	Donor top-hat	Acceptor top-hat	Acceptor tail
Energy level [eV]	−0.56	−0.20	0.20	0.56
Width [eV]	0.30	0.40	0.40	0.30

and acceptor-like defects were fit to match the asymmetry of the two sides of the curve; and the charge deviation σ_q was adjusted to control the broadness of the curve.

The fitted D_{it} and σ_n/σ_p at varying temperatures were then compared to the values reported in the literature.

3. Results and Discussion

3.1. Dielectric Layer with Positive Fixed Charges: SiO_2

The experimental τ_{eff} (at $\Delta n = 10^{15} \text{ cm}^{-3}$ and 25°C) of the SiO_2 sample as a function of the bias voltage is presented in Figure 4a. The top x -axis of this figure provides the charge as determined using Equation (3). The bias voltage range is divided into three regimes corresponding to the different behaviors of τ_{eff} . For the SiO_2 films with a positive fixed charge,^[6,53] n_s is dominant, creating an electron accumulation region at the Si/ SiO_2 interface (see the band diagram in Figure 4b). With positive bias voltages (Regime I), τ_{eff} significantly improves before saturation. This can be explained by the fact that the external positive bias voltage increases the dominance of n_s , resulting in an improvement of the asymmetry of the carrier populations and therefore a larger band bending at the interface (see Figure 4c).

With negative bias voltages, τ_{eff} significantly reduces (Regime II). This is because the external bias voltage neutralizes the potential caused by positive fixed charges in the SiO_2 films, leading to a decrease in n_s . This results in a reduction in the asymmetry of the carrier populations and the band bending at the Si/ SiO_2 interface as shown in the band diagram of Figure 4d. The τ_{eff} then reaches the minimum value at -3 V at which the flat band condition is achieved (see Figure 4e). It is assumed that at this point, the charge-assisted population control is minimal. The surface passivation at this point is solely provided by the chemical passivation. Hence, the two different passivation mechanisms at the Si/dielectric interface (chemical passivation and charge-assisted population control) can be separated in a simple and versatile manner. This allows assessing and comparing the chemical passivation quality of different dielectric films. The information gained from these measurements can be very useful for the optimization of the dielectric layers and the investigation of the fundamental properties of the passivation at the Si/dielectric layer interface. With further increasing the negative bias voltage, τ_{eff} dramatically increases as shown in Regime III. It is because p_s becomes dominant under sufficiently high negative bias voltage, resulting in a hole accumulation region at the Si/ SiO_2 interface (see the band diagram in Figure 4f). An imbalance of the carrier populations at this interface is once again achieved.

It is noteworthy that the experimental τ_{eff} as a function of bias voltage shows an asymmetry of two sides from the minimum τ_{eff} point. The surface carrier population is dominated by p_s on the left side and by n_s on the right side. The asymmetric V-shape in

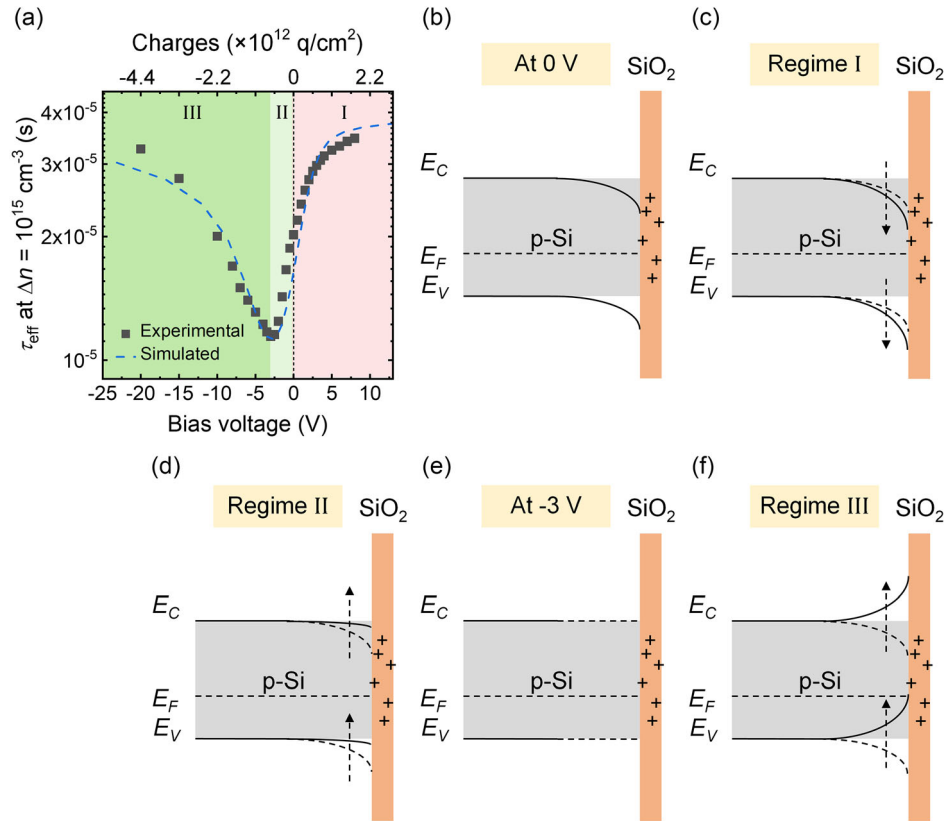


Figure 4. a) Experimental and simulated (dash line) τ_{eff} of the symmetrical lifetime test structure with SiO₂ films at $\Delta n = 10^{15}$ cm⁻³ and 25 °C as a function of bias voltage. The bias voltages were converted into charges using Equation (3) and are included in the top horizontal axis. b–f) Energy band diagrams of the test structure at 0 V, Regime I, Regime II, -3 V, and Regime III, respectively.

Figure 4a indicates an asymmetric σ_n/σ_p ratio. It is challenging to obtain information about the σ_n/σ_p ratio from common methods, for example, standard lifetime measurements.

As mentioned in Section 2.3, two input parameters can be extracted from τ_{eff} as a function of bias voltage measurements: $\tau_{\text{bulk,SRH}}$ and Q_f . In Regime I where τ_{eff} saturates, the surface passivation is maximized and τ_{eff} is dominated by bulk recombination while in Regime II (at a bias of -3 V) τ_{eff} is dominated by surface recombination. Hence, the bulk and surface contributions to τ_{eff} can be decoupled. This capability can be extremely useful for the investigation of the bulk without a strict requirement for excellent surface passivation at the initial state. The estimated $\tau_{\text{bulk,SRH}}$ of the SiO₂-based samples (52 ± 3 μ s; see Table 3) is low compared to current state-of-the-art bulk lifetimes.^[56,57] The

Table 3. Estimated $\tau_{\text{bulk,SRH}}$ by the bias voltage method, temporary passivation, and Quokka-based fitting; estimated (bias voltage method) and measured (contactless C–V) Q_f – SiO₂ sample.

	$\tau_{\text{bulk,SRH}}$ [μ s]	Q_f ($\times 10^{11}$ q cm ⁻²)
Bias voltage method	52 ± 3	3.5 ± 0.4
Temporary passivation method	77 ± 3	–
Quokka fit	71 ± 5	–
Contactless C–V	–	1.7 ± 0.6

low $\tau_{\text{bulk,SRH}}$ of the used p-type FZ wafers might be due to the inherent susceptibility of p-type Si wafers, even of FZ-grade quality, to impurity during high-temperature oxidation processes.^[58] To validate this estimate, we employed a temporary surface passivation method using a high concentration (50%) HF.^[59–65] Prior to applying the HF-based passivation, the metalized areas and all the other layers, including the PEDOT:PSS and SiO₂, were removed, followed by a comprehensive cleaning procedure.^[39] The τ_{eff} measurements were performed using a WCT-120TS lifetime tester (Sinton Instruments). Additionally, $\tau_{\text{bulk,SRH}}$ was estimated by the Quokka-based fitting method,^[66,67] with these values also summarized in Table 3. A reasonable agreement (within the range of 26–32%) between the three extracted $\tau_{\text{bulk,SRH}}$ is observed. The slightly lower $\tau_{\text{bulk,SRH}}$ value obtained by the proposed method might indicate that in cases where samples with extremely poor chemical surface passivation are measured, extracting the relative contributions of surface and bulk may lead to an underestimation of $\tau_{\text{bulk,SRH}}$. In these cases, the surface passivation is still impacted by the chemical passivation, even when it is subjected to very high voltages (Regime I). Additionally, the estimation of Q_f from Q_{gate} is compared to the value measured by the contactless C–V method, detailed in the same table. The higher estimated Q_f might arise from slight disparities in the insulator stack capacitance and/or Φ_{MS} , as compared to the values reported in ref. [38], which are utilized in this study.

Table 4. Best fit parameters, σ_n , σ_p , D_{it} , and σ_q , for donor- and acceptor-like defects and tail states in the SiO₂-based test structure. The D_{it} (at the middle of the Si bandgap) measured by the contactless C–V method is also included.

	Donor tail	Donor top-hat	Acceptor top-hat	Acceptor tail
D_{it} [cm ² ·eV ^{−1}]	$(3.1 \pm 0.3) \times 10^{16}$	$(2.0 \pm 0.2) \times 10^{11}$	$(2.0 \pm 0.2) \times 10^{11}$	$(1.0 \pm 0.3) \times 10^{15}$
D_{it} [cm ² ·eV ^{−1}] contactless C–V	–	$(1.2 \pm 0.3) \times 10^{11}$		–
σ_n [cm ²]	2.0×10^{-18}	2.51×10^{-16}	4.2×10^{-16}	2.0×10^{-18}
σ_p [cm ²]	2.0×10^{-18}	2.14×10^{-17}	8.7×10^{-16}	2.0×10^{-18}
σ_q [q cm ^{−2}]		1.0×10^{11}		

Using the input parameters listed in Table 2 and the extracted $\tau_{\text{bulk,SRH}}$ and Q_f , the D_{it} , σ_n/σ_p , and σ_q parameters were varied to fit the τ_{eff} as a function of bias voltage. Figure 4a illustrates the data and fits, demonstrating a great agreement (within 12%) between the experimental and simulated data. The fitted values are summarized in **Table 4**.

Table 4 includes the extracted D_{it} and compares them to the D_{it} measured by the contactless C–V method. The measured and fitted D_{it} values show good agreement with the same order of magnitude. This further supports the results obtained by the proposed model. **Table 5** compares the fitted σ_n/σ_p and those reported in the literature. While a wide range of values has been reported for σ_n , our fitted σ_n and σ_n/σ_p are in good agreement with the values reported in ref. [41].

The experimental τ_{eff} values measured from the symmetrical SiO₂ lifetime test structure at $\Delta n = 10^{15}$ cm^{−3} with increasing temperature are presented in **Figure 5**, as a function of bias voltage. At elevated temperatures, τ_{eff} shows a similar trend as at 25 °C, that is, V-shape curves. At any given bias voltage, τ_{eff} slightly increases with increasing temperature. As discussed above, at the minimum point, τ_{eff} is dominated by the chemical surface passivation. In this case, at a given E_b , only σ_n , σ_p , and D_{it} influence U_s . As D_{it} is hardly changed in the temperature range of 25–90 °C,^[53] the variation of τ_{eff} is probably due to the temperature dependence of interfacial σ_n and σ_p . Using our established model, σ_n and σ_p as a function of temperature are obtained and presented in **Figure 6a,b**. σ_n seems to be less sensitive to the temperature while σ_p exponentially increases and is estimated as

$\sigma_p = (0.2 \pm 0.01) \times 10^{-16} + 3.8 \times 10^{-4} \exp(T/15.4)$ cm². Similar temperature-dependent behavior for σ_p was recently reported by Nie et al.^[53]

To validate these fitted interfacial parameters, the experimental and simulated injection-dependent τ_{eff} at different temperatures and under various bias voltages are compared: 1) The minimum τ_{eff} points (−3 V for 25 °C and −2.5 V for 60 °C), where the flatband condition is expected to occur. At these points, the surface passivation relies solely on the chemical passivation, making τ_{eff} highly sensitive to the interfacial parameters and 2) At 0 V, representing the actual operating condition for solar cells in the field. Both at two different temperatures: 1) 25 °C, representing the standard testing conditions and 2) 60 °C, which closely mirrors the typical operating temperature in Australia.

The great agreement in high injections between the experimental and simulated lifetime curves, as shown in **Figure 7**, validates the fitted interfacial parameters obtained from the model. The slight mismatch between these curves at low injections can be attributed to the injection dependence of $\tau_{\text{bulk,SRH}}$. Note that there is more than one combination of the interfacial parameters that provide a good fit to τ_{eff} (at $\Delta n = 10^{15}$ cm^{−3}) as a function of bias voltage; however, it seems that there is only one combination that can simultaneously reproduce both the experimental injection-dependent τ_{eff} and the surface-potential-dependent τ_{eff} . The obtained σ_n and σ_p are critically important to gain a deeper understanding of surface recombination.

3.2. Dielectric Layer with Negative Fixed Charges: AlO_x

The measured τ_{eff} of the symmetrical lifetime test structure with AlO_x films at $\Delta n = 10^{15}$ cm^{−3} and 25 °C are presented in **Figure 8a** as a function of the bias voltage. The charges, converted from the bias voltages using Equation (3), are shown in the top horizontal axis of this figure. The bias voltage range in this figure is again divided into three regimes corresponding to the different behavior of the τ_{eff} . As AlO_x films are negatively charged,^[6] p_s is dominant, resulting in a hole accumulation region at the Si/AlO_x interface (see **Figure 8b**). With negative bias voltages, the τ_{eff} significantly increases before saturation, as shown in Regime I. It is because the external negative bias voltage increases the dominance of p_s , resulting in the improvement of the asymmetry of the carrier populations. This also leads to a more upward bend of the bands at the interface, as shown in **Figure 8c**.

As expected, the τ_{eff} significantly decreases (see Regime II) with increasing positive bias voltage since the external bias voltage neutralizes the potential caused by negative fixed charges in the AlO_x films, resulting in a decrease in p_s . This leads to the

Table 5. σ_n and σ_n/σ_p obtained from the model for the SiO₂-based test structure in this study and those reported in the literature.

References	σ_n/σ_p	σ_n [cm ²]	Substrate	ρ [Ω·cm]	Method
This study	11.2	$(1.2 \pm 0.3) \times 10^{-16}$	p-type FZ	1–2	PC
[53]	2	$(1.4 \pm 0.4) \times 10^{-16}$	n-type FZ	1	PC
[53]	2	1.4×10^{-16}	n-type FZ	1	PC
[36]	2.3	7.5×10^{-15}	n-type FZ	2–3	PL
[36]	5.2	1.5×10^{-14}	p-type FZ	2–3	PL
[41]	7.9	8.7×10^{-16}	n-type	1	PC
[41]	13.4	7.7×10^{-16}	n-type	1	PC
[68]	50–70	–	p-type	1	DLTS and C–V

PL: Photoluminescence.

DLTS: Deep-level transient spectroscopy.

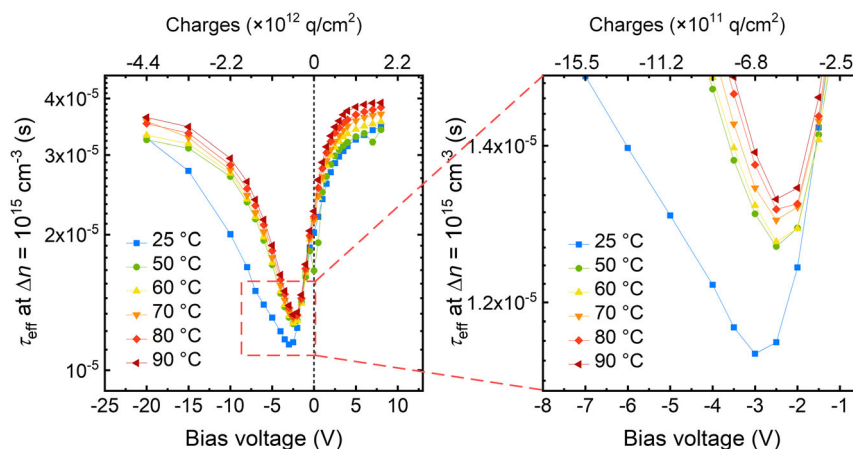


Figure 5. Experimental τ_{eff} of the symmetrical lifetime test structure with SiO_2 films at $\Delta n = 10^{15} \text{ cm}^{-3}$ in the temperature range of 25–90 °C as a function of bias voltage. The charges converted from the bias voltages using Equation (3) are shown on the top axis.

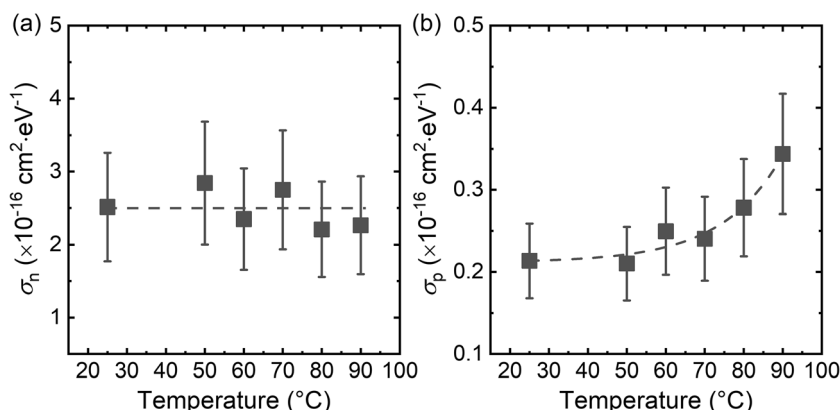


Figure 6. a) σ_n and σ_p at the Si/SiO_2 interface as a function of temperature.

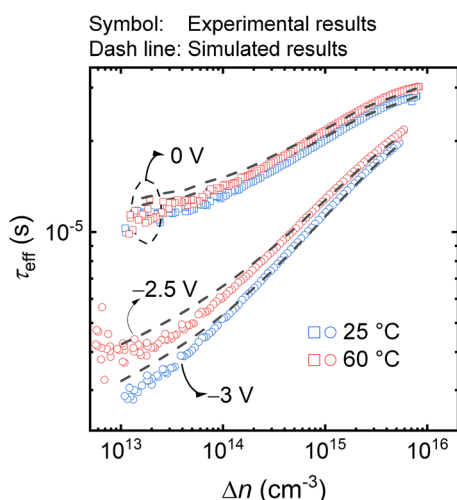


Figure 7. Experimental (symbol) and simulated (dash line) lifetime curves of the symmetrical SiO_2 lifetime test structure at different temperatures and under various bias voltages.

attenuation of the asymmetry of the carrier populations and of the band bending at the Si/AlO_x interface as shown in the band diagram in Figure 8d. The τ_{eff} then reaches the minimum value at 6 V at which the flat band condition is expected to occur (see the band diagram in Figure 8e). Again, the two different passivation mechanisms at Si/AlO_x (chemical passivation and charge-assisted population control) can be separated as the surface passivation is expected to solely result from the chemical passivation. With a further increase in positive bias voltage, τ_{eff} remarkably improves as shown in Regime III. This is due to n_s becoming dominant under sufficiently high positive bias voltage, resulting in an electron accumulation region at the Si/AlO_x interface (see the band diagram in Figure 8f). An imbalance of the carrier populations at this interface is once again achieved.

The $\tau_{\text{bulk,SRH}}$ and Q_f were estimated from τ_{eff} as a function of bias voltage and used as input parameters for the simulations. The estimated $\tau_{\text{bulk,SRH}}$ was also compared to the values obtained from the temporary HF passivation and the Quokka-based fitting method, as summarized in Table 6. It is evident that the obtained $\tau_{\text{bulk,SRH}}$ are in good agreement with each other (within the range

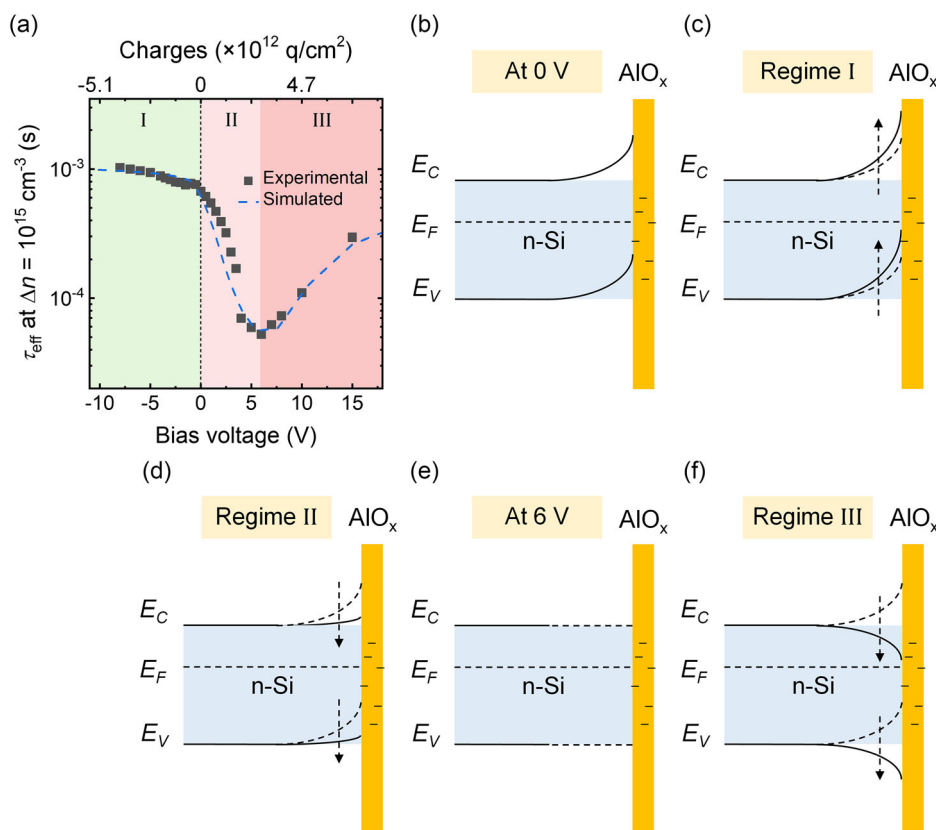


Figure 8. a) Experimental and simulated (dash line) τ_{eff} of the symmetrical lifetime test structure with AlO_x films at $\Delta n = 10^{15} \text{ cm}^{-3}$ and 25°C as a function of bias voltage. The bias voltages were converted into charges using Equation (3) and are included in the top horizontal axis. b–f) Energy band diagrams of the test structure at 0 V, Regime I, Regime II, 6 V, and Regime III, respectively.

Table 6. Estimated $\tau_{\text{bulk,SRH}}$ by the bias voltage method, temporary passivation, and Quokka-based fitting; estimated (bias voltage method) and measured (contactless C–V) Q_f – AlO_x sample.

	$\tau_{\text{bulk,SRH}}$ [μs]	Q_f ($\times 10^{12} \text{ q cm}^{-2}$)
Bias voltage method	1090 ± 19	-2.2 ± 0.2
Temporary passivation method	1232 ± 37	–
Quokka fit	954 ± 26	–
Contactless C–V	–	$-(1.4 \pm 0.2)$

of 11–12%), reaffirming the effectiveness of the proposed method in estimating $\tau_{\text{bulk,SRH}}$. Similarly, the estimated Q_f from Q_{gate} was compared with the measured Q_f via the contactless C–V method in the same table. The potential reasons for the slight discrepancy between these values were discussed above (refer to Section 3.1).

The simulated τ_{eff} values at $\Delta n = 10^{15} \text{ cm}^{-3}$ and 25°C are depicted in Figure 8a, with the corresponding parameters, σ_n , σ_p , D_{it} , and σ_q , summarized in Table 7. The simulated and experimental τ_{eff} curves match well (within 15%).

The D_{it} measured by the contactless C–V method is also shown in Table 7 for comparison. The measured and fitted

Table 7. Best fit parameters, σ_n , σ_p , D_{it} , and σ_q , for donor- and acceptor-like defects and tail states in the AlO_x -based test structure. The D_{it} (at the middle of the Si bandgap) measured by the contactless C–V method is also included.

	Donor tail	Donor top-hat	Acceptor top-hat	Acceptor tail
D_{it} [$\text{cm}^{-2} \text{ eV}^{-1}$]	3.0×10^{14}	2.0×10^{10}	2.0×10^{10}	4.0×10^{14}
D_{it} [$\text{cm}^{-2} \text{ eV}^{-1}$] contactless C–V	–	$(3.4 \pm 0.9) \times 10^{10}$		–
σ_n [cm^2]	1.0×10^{-18}	1.4×10^{-16}	9.0×10^{-17}	1.0×10^{-18}
σ_p [cm^2]	1.0×10^{-18}	8.5×10^{-17}	7.0×10^{-16}	1.0×10^{-18}
σ_q [q cm^{-2}]	8.0×10^{11}			

D_{it} values show good agreement with the same order of magnitude, supporting the results obtained from the model. The σ_n and σ_n/σ_p obtained from the model in this study are compared to those presented in our recently published study^[8] and reported in the literature. All the values are summarized in Table 8. All the σ_n and σ_p values in this table are different compared to each other, but not more than one order of magnitude. Note that the AlO_x films of the test structures

Table 8. σ_n , σ_p , and σ_n/σ_p obtained from the model for the AlO_x -based test structure in this study and those reported in the literature.

Defect	Parameter	This study	[8]	[69]	[70]
	Substrate	n-type CZ	n-type CZ	p-type CZ	p-type Fz
	ρ [$\Omega\cdot\text{cm}$]	8–10	5.8–6.4	6–8	1.3–1.5
	Method	PECVD	ALD	APCVD	PAALD
Donor-like	σ_n [cm^2]	1.4×10^{-16}	4.0×10^{-15}	1.8×10^{-14}	–
	σ_p [cm^2]	8.5×10^{-17}	4.0×10^{-16}	1.3×10^{-16}	$(4 \pm 3) \times 10^{-16}$
	σ_n/σ_p	2	10	138	–
Acceptor-like	σ_n [cm^2]	9.0×10^{-17}	1.0×10^{-15}	1.0×10^{-16}	$(7 \pm 4) \times 10^{-15}$
	σ_p [cm^2]	7.0×10^{-16}	2.6×10^{-14}	2.0×10^{-14}	–
	σ_n/σ_p	0.1	0.04	0.005	–

APCVD: Atmospheric pressure chemical vapor deposition.
PAALD: Plasma-assisted atomic layer deposition.

presented in Table 8 were prepared by different deposition methods. This might lead to the different nature of the interfacial defects, which may explain the difference in σ_n and σ_p .

The measured τ_{eff} of the symmetrical lifetime test structure with AlO_x films at $\Delta n = 10^{15} \text{ cm}^{-3}$ with increasing temperature is presented in Figure 9 as a function of bias voltage. At elevated temperatures, τ_{eff} shows a similar trend as a function of the bias voltage. At a given negative bias voltage, τ_{eff} slightly increases with increasing temperature, similar to the SiO_2 -based test structure. It is noteworthy that the minimum τ_{eff} varies with temperature, indicating the temperature dependence of interfacial σ_n and σ_p , as discussed above for the SiO_2 -based test structure. Using our established model, σ_n and σ_p as a function of temperature are obtained and presented in Figure 10a,b. The σ_n exponentially increases and is estimated as $\sigma_n = (1.6 \pm 0.1) \times 10^{-16} + 1.0 \times 10^{-4} \exp(T/9.1) \text{ cm}^2$ while σ_p seems to be less sensitive to the temperature in that range.

A similar approach as presented in the previous section is used to validate the fitted interfacial parameters. The τ_{eff} as a function of Δn at 25 and 60 °C under the bias voltages of 0 and 6 V is simulated. A reasonable match between the experimental and simulated lifetime curves is obtained as shown in Figure 11, confirming the general validity of the fitted interfacial parameters obtained from our model.

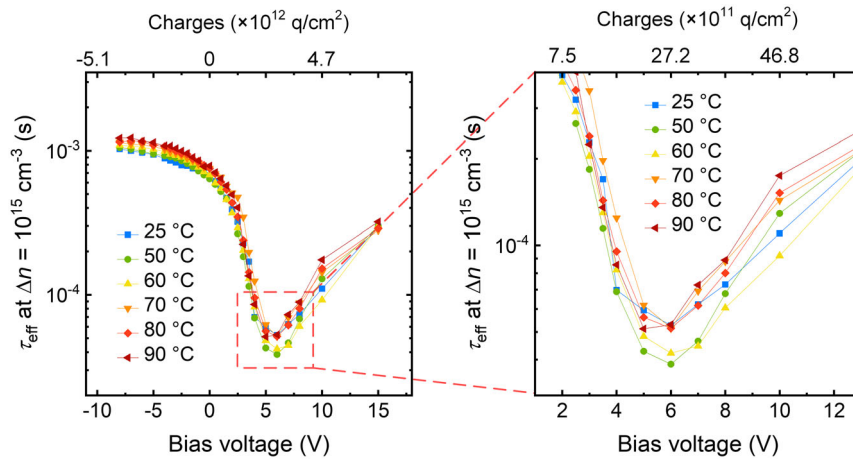


Figure 9. Experimental τ_{eff} of the symmetrical lifetime test structure with AlO_x films at $\Delta n = 10^{15} \text{ cm}^{-3}$ in the temperature range of 25–90 °C as a function of bias voltage. The bias voltages were converted into charges using Equation (3) and are included in the top axis.

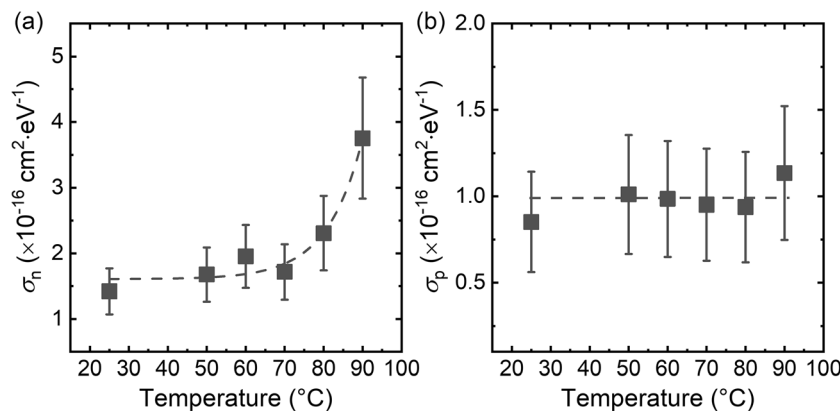


Figure 10. a) σ_n and b) σ_p at the Si/AlO_x interface as a function of temperature.

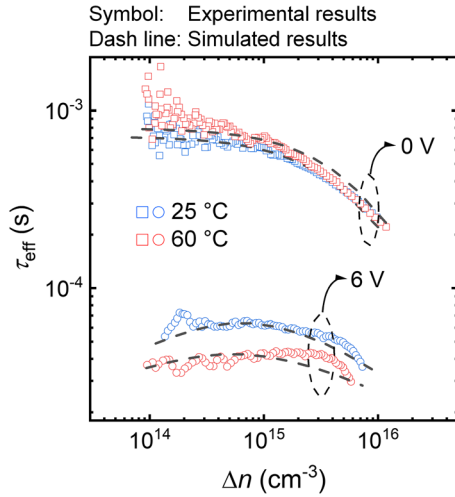


Figure 11. Experimental (symbol) and simulated (dash line) lifetime curves of the symmetrical AlO_x lifetime test structure at different temperatures and under various bias voltages.

4. Conclusion

In this study, we probed the temperature-dependent recombination dynamics at the SiO_2/Si and AlO_x/Si interfaces using advanced measurement and modeling techniques. Manipulating carrier populations near the Si surfaces by varying external bias voltages unveiled important insights into the recombination behavior at these critical interfaces. This approach provides multifaceted capabilities as follows: 1) The separation of the chemical passivation and charge-assisted population control at the Si/dielectric interface; 2) The evaluation and comparison of the chemical passivation quality across different dielectric films; 3) The extraction of Q_f , σ_n , and σ_p ; and 4) The decoupling of the bulk and surface contributions to the τ_{eff} and, hence, the estimation of the $\tau_{\text{bulk,SRH}}$ in most practical cases. However, in situations where the chemical surface passivation is extremely poor, extracting the relative contributions of surface and bulk may lead to a slight underestimation of $\tau_{\text{bulk,SRH}}$.

More importantly, these capabilities and important information can be obtained at different temperatures. Based on the proposed model, the temperature dependence of σ_n and σ_p for both the $\text{SiO}_2/\text{c-Si}$ and $\text{AlO}_x/\text{c-Si}$ interfaces is obtained and defined as: 1) $\text{SiO}_2/\text{c-Si}$ interface: $\sigma_p = (0.2 \pm 0.01) \times 10^{-16} + 3.8 \times 10^{-4} \exp(T/15.4) \text{ cm}^2$ while σ_n seems to be less sensitive to the temperature. 2) $\text{AlO}_x/\text{c-Si}$ interface: $\sigma_n = (1.6 \pm 0.1) \times 10^{-16} + 1.0 \times 10^{-4} \exp(T/9.1) \text{ cm}^2$ while σ_p seems to be less sensitive to the temperature.

The information regarding the temperature-dependent capture cross sections is fundamental to accurately reproduce the experimental data under realistic field operating temperatures. The capability to provide such information will significantly improve the understanding of the Si/dielectric interface. These findings underscore the substantial potential of this method in comprehensively probing recombination statistics at Si interfaces, offering valuable insights for further advancements in the passivation of next-generation commercial Si solar cells.

Appendix A: Determination of the Thermal Velocity of Carriers

The ν_{thn} and ν_{thp} are determined by^[47,48]

$$\nu_{\text{thn}} = (8kT/\pi m_{\text{tc}})^{1/2} \quad (\text{A1})$$

$$\nu_{\text{thp}} = (8kT/\pi m_{\text{td}})^{1/2} \quad (\text{A2})$$

where m_{tc} and m_{td} are the thermal velocity effective masses of carriers for the conduction and valence bands, respectively. They are defined by

$$m_{\text{tc}} = \frac{4m_l}{(1 + (m_l/m_t)^{1/2} \sin^{-1}(\delta)/\delta)^2} \quad (\text{A3})$$

$$m_{\text{td}} = m_e \left(\frac{a + bT + cT^2 + dT^3 + eT^4}{1 + fT + gT^2 + hT^3 + iT^4} \right)^{2/3} \quad (\text{A4})$$

$$\delta^2 = (m_l - m_t)/m_l \quad (\text{A5})$$

$$m_l = 0.9163 \times m_e \text{ and } m_t = 0.1905 \times m_e \times E_{g0}/E_g(T) \quad (\text{A6})$$

where m_l and m_t are the longitudinal and transverse effective masses associated with the ellipsoidal constant energy surfaces, and m_e is the electron rest mass. All the coefficients and parameters in Equation (A4) can be found in Table 4 in ref. [47] and in Table 3 in ref. [48].

Appendix B: Defect Distributions

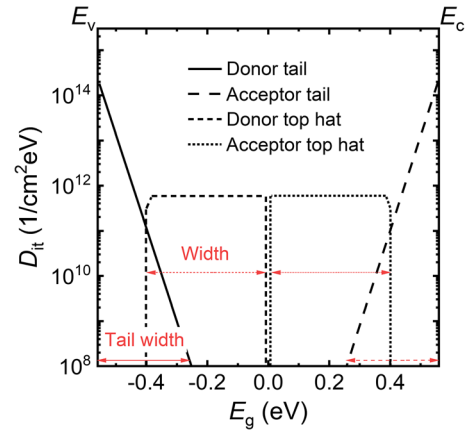


Figure 1B. The distribution of defects including donor tail, acceptor tail, donor top-hat, and acceptor top-hat.

Acknowledgements

The authors thank Nitin Nampalli and Padhamnath Pradeep from the Solar Energy Research Institute of Singapore (SERIS) for their valuable assistance in sample preparation. This work was supported by the Australian Government through the Australian Renewable Energy Agency [ARENA; project 2022/TRAC001]. R.S.B. was supported by the UK Royal Academy of Engineering under the Research Fellowship Scheme (RF\201819\18\38).

The views expressed herein are not necessarily the views of the Australian Government, and the Australian Government does not accept responsibility for any information or advice contained herein.

Conflict of Interest

The authors declare no conflict of interest.

Data Availability Statement

The data that support the findings of this study are available from the corresponding author upon reasonable request.

Keywords

capture cross sections, dielectric films, recombinations, surface passivations, temperature dependences

Received: March 6, 2024

Revised: June 28, 2024

Published online: September 2, 2024

- [1] M. A. Green, *Englewood Cliffs*, Prentice-Hall, NJ, USA **1982**.
- [2] Y. Zhang, N. Stokes, B. Jia, S. Fan, M. Gu, *Sci. Rep.* **2014**, *4*, 1.
- [3] H. Sai, Y. Sato, T. Oku, T. Matsui, *Prog. Photovolt.: Res. Appl.* **2021**, *29*, 1093.
- [4] Y. Yang, A. Yu, B. Hsu, W. Hsu, A. Yang, C. Lan, *Prog. Photovolt.: Res. Appl.* **2015**, *23*, 340.
- [5] C. Battaglia, A. Cuevas, S. De Wolf, *Energy Environ. Sci.* **2016**, *9*, 1552.
- [6] R. S. Bonilla, B. Hoex, P. Hamer, P. R. Wilshaw, *Physica Status Solidi A* **2017**, *214*, 1700293.
- [7] A. Cuevas, Y. Wan, D. Yan, C. Samundsett, T. Allen, X. Zhang, J. Cui, J. Bullock, *Sol. Energy Mater. Sol. Cell* **2018**, *184*, 38.
- [8] A. H. T. Le, R. S. Bonilla, L. E. Black, J. P. Seif, T. G. Allen, R. Dumbrell, C. Samundsett, Z. Hameiri, *Sol. RRL* **2022**, *7*, 2201050.
- [9] M. Green, A. Blakers, J. Shi, E. Keller, S. Wenham, *Appl. Phys. Lett.* **1984**, *44*, 1163.
- [10] Z. Wang, P. Han, H. Lu, H. Qian, L. Chen, Q. Meng, N. Tang, F. Gao, Y. Jiang, J. Wu, W. Wu, H. Zhu, J. Ji, Z. Shi, A. Sugianto, L. Mai, B. Hallam, S. Wenham, *Prog. Photovolt.: Res. Appl.* **2012**, *20*, 260.
- [11] S. Zhang, X. Pan, H. Jiao, W. Deng, J. Xu, Y. Chen, P. P. Altermatt, Z. Feng, P. J. Verlinden, *IEEE J. Photovolt.* **2015**, *6*, 145.
- [12] J. Zhao, A. Wang, M. A. Green, *Prog. Photovolt.: Res. Appl.* **1999**, *7*, 471.
- [13] J. Zhao, A. Wang, M. A. Green, *Sol. Energy Mater. Sol. Cell.* **2001**, *65*, 429.
- [14] K. H. Kim, C. S. Park, J. D. Lee, J. Y. Lim, J. M. Yeon, I. H. Kim, E. J. Lee, Y. H. Cho, *Jpn J. Appl. Phys.* **2017**, *56*, 08MB25.
- [15] J. Haynos, J. Allison, R. Arndt, A. Meulenbergh, in *Proc. of the Int. Conf.*, Hamburg, Germany, September **1974**, p. 487.
- [16] Z. Hameiri, L. Mai, A. Sproul, S. Wenham, *Appl. Phys. Lett.* **2010**, *97*, 222111.
- [17] T. Dullweber, C. Kranz, B. Beier, B. Veith, J. Schmidt, B. F. P. Roos, O. Hohn, T. Dippell, R. Brendel, *Sol. Energy Mater. Sol. Cell.* **2013**, *112*, 196.
- [18] A. To, S. Tahir, A. Garavaglia, W.-M. Li, X. Li, B. Hoex, *IEEE J. Photovolt.* **2017**, *7*, 1528.
- [19] D. Garcia-Alonso, S. Smit, S. Bordihn, W. Kessels, *Semicond. Sci. Technol.* **2013**, *28*, 082002.
- [20] C. Reichel, F. Feldmann, A. Richter, J. Benick, M. Hermle, S. W. Glunz, *Prog. Photovolt.: Res. Appl.* **2022**, *30*, 288.
- [21] S. L. Pain, E. Khorani, T. Niewelt, A. Wratten, G. J. Paez Fajardo, B. P. Winfield, R. S. Bonilla, M. Walker, L. F. J. Piper, N. E. Grant, J. D. Murphy, *Adv. Mater. Interfaces* **2022**, 2201339.
- [22] E. Khorani, S. McNab, T. E. Scheul, T. Rahman, R. S. Bonilla, S. A. Boden, P. R. Wilshaw, *APL Mater.* **2020**, *8*, 111106.
- [23] Z. P. Ling, Z. Xin, G. Kaur, C. Ke, R. Stangl, *Sol. Energy Mater. Sol. Cell.* **2018**, *185*, 477.
- [24] D. Zielke, J. H. Petermann, F. Werner, B. Veith, R. Brendel, J. Schmidt, *Phys. Status Solidi–Rap. Res. Lett.* **2011**, *5*, 298.
- [25] F. Feldmann, M. Simon, M. Bivour, C. Reichel, M. Hermle, S. W. Glunz, *Appl. Phys. Lett.* **2014**, *104*, 181105.
- [26] J. Schmidt, A. G. Aberle, *Prog. Photovolt.: Res. Appl.* **1998**, *6*, 259.
- [27] R. S. Bonilla, C. Reichel, M. Hermle, P. Hamer, P. R. Wilshaw, *Appl. Surf. Sci.* **2017**, *412*, 657.
- [28] G. Dingemans, M. Van de Sanden, W. Kessels, *Electrochem. Solid-State Lett.* **2009**, *13*, H76.
- [29] T. C. Kho, S. C. Baker-Finch, K. R. McIntosh, *J. Appl. Phys.* **2011**, *109*, 053108.
- [30] S. Glunz, D. Biro, S. Rein, W. Warta, *J. Appl. Phys.* **1999**, *86*, 683.
- [31] P. M. Jordan, D. K. Simon, T. Mikolajick, I. Dirnstorfer, *Appl. Phys. Lett.* **2015**, *106*, 061602.
- [32] P. M. Jordan, D. K. Simon, F. P. Fengler, T. Mikolajick, I. Dirnstorfer, *Energy Procedia* **2015**, *77*, 91.
- [33] W. E. Jellett, K. Weber, *Appl. Phys. Lett.* **2007**, *90*, 042104.
- [34] E. Yablonovitch, R. Swanson, W. Eades, B. Weinberger, *Appl. Phys. Lett.* **1986**, *48*, 245.
- [35] R. B. Girisch, R. P. Mertens, R. F. De Keersmaecker, *IEEE Trans. Electron. Dev.* **1988**, *35*, 203.
- [36] H. Haug, S. Olibet, Ø. Nordseth, E. Stensrud Marstein, *J. Appl. Phys.* **2013**, *114*, 174502.
- [37] H. Haug, Ø. Nordseth, E. V. Monakhov, E. S. Marstein, *Sol. Energy Mater. Sol. Cell.* **2012**, *106*, 60.
- [38] R. S. Bonilla, *Sol. RRL* **2018**, *2*, 1800172.
- [39] W. Kern, *J. Electrochem. Soc.* **1990**, *137*, 1887.
- [40] A. H. T. Le, E. P. Ochoa, R. S. Bonilla, N. Borojevic, Z. Hameiri, in *49th IEEE Photovoltaics Specialists Conf.*, Philadelphia, USA, June **2022**, pp. 0443–0443.
- [41] R. S. Bonilla, I. Al-Dhahir, M. Yu, P. Hamer, P. P. Altermatt, *Sol. Energy Mater. Sol. Cell.* **2020**, *215*, 110649.
- [42] A. Grove, D. Fitzgerald, *Solid State Electron.* **1966**, *9*, 783.
- [43] A. G. Aberle, S. Glunz, W. Warta, *J. Appl. Phys.* **1992**, *71*, 4422.
- [44] C. E. Young, *J. Appl. Phys.* **1961**, *32*, 329.
- [45] S. Rein, *Lifetime Spectroscopy: A Method Of Defect Characterization in Silicon for Photovoltaic Applications*, Springer Science & Business Media, Berlin **2006**.
- [46] R. Couderc, M. Amara, M. Lemiti, *J. Appl. Phys.* **2014**, *115*, 093705.
- [47] R. Humphreys, *J. Phys. C: Solid State Phys.* **1981**, *14*, 2935.
- [48] M. A. Green, *J. Appl. Phys.* **1990**, *67*, 2944.
- [49] K. R. McIntosh, S. C. Baker-Finch, N. E. Grant, A. F. Thomson, S. Singh, I. D. Baikié, *J. Electrochem. Soc.* **2009**, *156*, G190.
- [50] A. G. Aber, S. Glunz, W. Warta, *Sol. Energy Mater. Sol. Cell.* **1993**, *29*, 175.
- [51] R. S. Bonilla, P. R. Wilshaw, *J. Appl. Phys.* **2017**, *121*, 135301.
- [52] M. Wilson, J. Lagowski, L. Jastrzebski, A. Savtchouk, V. Faifer, in *AIP Conf. Proc.*, Maryland, USA, June **2001**, Vol. 550, pp. 220–225.
- [53] S. Nie, R. S. Bonilla, Z. Hameiri, *Sol. Energy Mater. Sol. Cell.* **2021**, *224*, 111021.
- [54] M. Yu, S. McNab, I. Al-Dhahir, C. E. Patrick, P. P. Altermatt, R. S. Bonilla, *Sol. Energy Mater. Sol. Cell.* **2021**, *231*, 111307.
- [55] Y. Etinger-Geller, E. Zoubenko, M. Baskin, L. Kornblum, B. Pokroy, *J. Appl. Phys.* **2019**, *125*, 185302.

- [56] Y. Zhang, L. Wang, D. Chen, M. Kim, B. Hallam, *J. Phys. D: Appl. Phys.* **2021**, *54*, 214003.
- [57] A. Augusto, J. Karas, P. Balaji, S. Bowden, R. King, *J. Mater. Chem. A* **2020**, *8*, 16599.
- [58] N. E. Grant, V. P. Markevich, J. Mullins, A. R. Peaker, F. Rougieux, D. Macdonald, J. D. Murphy, *Phys. Status Solidi A* **2016**, *213*, 2844.
- [59] E. Yablonovitch, D. Allara, C. Chang, T. Gmitter, T. Bright, *Phys. Rev. Lett.* **1986**, *57*, 249.
- [60] K. L. Luke, L. J. Cheng, *J. Electrochem. Soc.* **1988**, *135*, 957.
- [61] N. E. Grant, K. R. McIntosh, J. T. Tan, *ECS J. Solid State Sci. Technol.* **2012**, *1*, P55.
- [62] D. J. Michalak, F. Gstrein, N. S. Lewis, *J. Phys. Chem. C* **2008**, *112*, 5911.
- [63] R. A. Razera, A. Moehlecke, I. Zanesco, *IEEE J. Photovolt.* **2017**, *7*, 1004.
- [64] H. M'saad, J. Michel, J. Lappe, L. Kimerling, *J. Electron. Mater.* **1994**, *23*, 487.
- [65] N. E. Grant, J. D. Murphy, *Phys. Status Solidi–Rap. Res. Lett.* **2017**, *11*, 1700243.
- [66] A. Fell, *IEEE Trans. Electron. Dev.* **2013**, *60*, 733.
- [67] R. Dumbrell, M. K. Juhl, T. Trupke, Z. Hameiri, *IEEE J. Photovolt.* **2018**, *8*, 1413.
- [68] A. Aberle, S. Glunz, A. Stephens, M. Green, *Prog. Photovolt.: Res. Appl.* **1994**, *2*, 265.
- [69] L. E. Black, K. R. McIntosh, *IEEE J. Photovolt.* **2013**, *3*, 936.
- [70] P. Saint-Cast, Y.-H. Heo, E. Billot, P. Olwal, M. Hofmann, J. Rentsch, S. W. Glunz, R. Preu, *Energy Procedia* **2011**, *8*, 642.